Environmental Science
Processes & Impacts

Crystal lattice defects in nanocrystalline metacinnabar in contaminated streambank soils indicate a role for biogenic sulfides in the formation of mercury sulfide phases

Journal:	*Environmental Science: Processes & Impacts*
Manuscript ID	EM-ART-12-2021-000549.R1
Article Type:	Paper

Environmental Significance:
Erosion from contaminated streambank soils can serve as the primary source of mercury input to freshwater stream systems. Identifying the solid phase speciation and processes that control mercury release from eroded soil is critical for predicting mercury fate. Here we determine that large aggregates enriched in mercury and sulfur particles present in oxic contaminated streambank soils are the result of clusters of nanocrystalline mercury sulfide. The undercoordinated nanocrystalline mercury sulfide structure is the result of crystallographic defects. Unraveling the importance of crystal defects on nanoparticle reactivity is important for making accurate predictions of mercury mobilization and bioavailability.

Crystal lattice defects in nanocrystalline metacinnabar in contaminated streambank soils suggest a role for biogenic sulfides in the formation of mercury sulfide phases

Faye Koenigsmark[1], Michelle Chiu[2], Nelson Rivera[1], Alexander Johs[2], Jeremy Eskelsen[2], Donovan Leonard[3], Boakai K. Robertson[4], Anna Szynkiewicz[5], Christopher Derolph[2], Linduo Zhao[2], Baohua Gu[2], Heileen Hsu-Kim[1], Eric M. Pierce[2]*

[1]Civil and Environmental Engineering, Duke University, Durham, NC 27708, USA
[2]Environmental Sciences Division, Oak Ridge National Laboratory, Oak Ridge, TN 37831, USA
[3]Manufacturing Demonstration Facility Division, Oak Ridge National Laboratory, Oak Ridge, TN 37831, USA
[4]Department of Biological Sciences, Alabama State University, Montgomery, AL 36104, USA
[5]Department of Earth and Planetary Sciences, University of Tennessee at Knoxville, Knoxville, TN 37996, USA

Keywords: nanocrystalline metacinnabar, spectroscopy, mercury, speciation

***Corresponding author**: Phone: 865-574-9968, Email: pierceem@ornl.gov

Notice: This manuscript has been authored by UT-Battelle, LLC, under contract DE-AC05-00OR22725 with the US Department of Energy (DOE). The US government retains and the publisher, by accepting the article for publication, acknowledges that the US government retains a nonexclusive, paid-up, irrevocable, worldwide license to publish or reproduce the published form of this manuscript, or allow others to do so, for US government purposes. DOE will provide public access to these results of federally sponsored research in accordance with the DOE Public Access Plan (https://energy.gov/downloads/doe-public-access-plan).

Abstract

At mercury (Hg)-contaminated sites, streambank erosion can act as a main mobilizer of Hg into nearby waterbodies. Once deposited into the waters, mercury from these soils can be transformed to MeHg by microorganisms. It is therefore important to understand the solid-phase speciation of Hg in streambanks as differences in Hg speciation will have implications for Hg transport and bioavailability. In this study, we characterized Hg solid phases in Hg-contaminated soils (100–1100 mg/kg Hg) collected from the incised bank of the East Fork Poplar Creek (EFPC) in Oak Ridge, TN (USA). The analysis of the soil samples by scanning electron microscopy-energy dispersive spectroscopy indicated numerous microenvironments where Hg and sulfur (S) are co-located. According to bulk soil analyses by extended X-ray absorption fine structure spectroscopy (EXAFS), the near-neighbor Hg molecular coordination in the soils closely resembled freshly precipitated Hg sulfide (metacinnabar, HgS); however, EXAFS fits indicated the Hg in the HgS structure was undercoordinated with respect to crystalline metacinnabar. This undercoordination of Hg-S observed by spectroscopy is consistent with transmission electron microspy images showing the presence of nanocrystallites with structural defects (twinning, stacking faults, dislocations) in individual HgS-bearing particles. Although the soils were collected from exposed parts of the stream bank (i.e., open to the atmosphere), the presence of reduced forms of S and sulfate-reducing microbes suggests that biogenic sulfides promote the formation of HgS nanoparticles in these soils. Altogether, these data demonstrate the predominance of nanoparticulate HgS with crystal lattice defects in the bank soils of an industrially impacted stream. Efforts to predict the mobilization and bioavailability of Hg associated with nano-HgS forms should consider the impact of nanocrystalline lattice defects on particle surface reactivity, including Hg dissolution rates and bioavailability on Hg fate and transformations.

1. Introduction

Soils in riparian zones of watersheds act as an important repository for metals through adsorption and sedimentation processes.[1-3] The accumulation and retention of metals in these soils largely depend on localized geochemical conditions and how those conditions influence metal speciation.[4, 5] In particular, the dynamic hydrologic behavior within riparian soils creates conditions that strongly impact metal cycling. Fluctuating redox state caused by flooding events can temporarily create sulfate-reducing conditions ideal for metal sequestration via precipitation as metal sulfides.[6-8] Particularly in the case of mercury (Hg), the formation of sparingly soluble mercury sulfides (HgS) may reduce microbial production of methylmercury (MeHg), a bioaccumulative neurotoxin.[9, 10]

East Fork Poplar Creek (EFPC) in Oak Ridge, Tennessee, (USA) is one example of a highly contaminated riparian zone in the United States. EFPC was placed on the US Environmental Protection Agency's National Priorities List of Superfund sites in 1989 because of extensive Hg contamination resulting from historical activities at the US Department of Energy's Y-12 National Security Complex (Y-12 NSC).[11] From 1950 to 1963, the Y-12 NSC, located at the headwaters of the EFPC, was the site for substantial usage of liquid elemental Hg (Hg^0_L) for the separation of lithium (Li) isotopes.[12] Unintended spills, leaks, and discharge during this time resulted in an estimated 385 tons of Hg lost to the local environment,[13, 14] which contaminated the terrestrial and aquatic compartments of the EFPC watershed. Similar to the Y-12 NSC, other locations hosting historical and ongoing usage of Hg^0_L for industrial processing[15-17] and gold mining[18-22] have experienced large-scale Hg releases to local riparian ecosystems.

The riparian soils of the EFPC can generally be grouped into streambank (SB) soils and floodplain soils. SB soils are proximally located (i.e., within 1 m) and exposed to the stream while floodplain soils are located upland and contribute solutes and particles to the stream via overland and subsurface flows. The extent of our knowledge of metal sulfide formation, in particular HgS, in these soils is somewhat limited. Sequestration of chalcophile metals as metal sulfides is expected to occur in anoxic sediments and porewater[23-27] and in estuarine settings with high concentrations of available sulfur for sulfidation reactions.[28-30] Unlike these settings, riparian soils generally have moderate to low amounts of available sulfide.[8, 31] Although the speciation and geochemical reactivity of Hg and other metals in floodplain soils has been investigated in numerous locations[6, 8, 32-34], most studies rely on sequential extractions or other non-spectroscopic characterization methods that provide limited insights at the molecular scale. Only a few studies have characterized Hg speciation in floodplain soils under oxic conditions, and they have confirmed the formation of HgS particles.[35, 36] The mechanism of sulfide formation in these oxic soil settings is not entirely clear; both biotic (i.e., microbial sulfate reduction during flooding) and abiotic (i.e., transformation of Hg(II)-thiolate complexes in organic matter) processes have been proposed.[35, 36] The mode of HgS particle formation guides the crystal structure and interfacial composition that can influence surface interactions with other particles, mobilization, and bioavailablity potential of Hg in the stream.

Although much emphasis has been placed on floodplain soils in the study of Hg inputs to stream ecosystems near these industrially impacted sites, an equally important compartment of the riparian zone are SB soils, which serve as the interface between the stream and upland terrain.[37-39] Streambanks are particularly important because of their potential to erode over time, serving as direct input of Hg into water bodies where transformation to MeHg is possible. In fact, research quantifying Hg inputs to EFPC revealed SB erosion to be the most significant loading input of Hg to the creek, whereas the floodplain contribution was minimal.[14, 40] Therefore, in this work, we sought to evaluate the speciation of Hg in bank soils of EFPC as a means for understanding the historical mode of Hg accumulation in stream banks and future potential for transformation as bank soils are eroded.

In this research, we focused on a subset of SB soils as part of a larger study characterizing Hg and MeHg distributions along the creek.[15, 41] Prior selective sequential extractions of a subset of samples suggest that 89.3% ± 5.6% of the Hg was extracted with aqua regia (F5 fraction),[42] which is consistent with the most recalcitrant Hg phases, such as HgS.[15] These extractions provide an idea of the biogeochemically relevant fractions, but there are limits in interpretation when fractionating a sample into operationally defined groups based on extraction media.[43-46] To overcome the limitations of previous analyses, we used a variety of characterization approaches, including elemental analyses, electron microscopy, X-ray absorption spectroscopy, and microbial community analysis to characterize the structure and orgins of nanocrystalline HgS (nano-HgS) in bank soils.

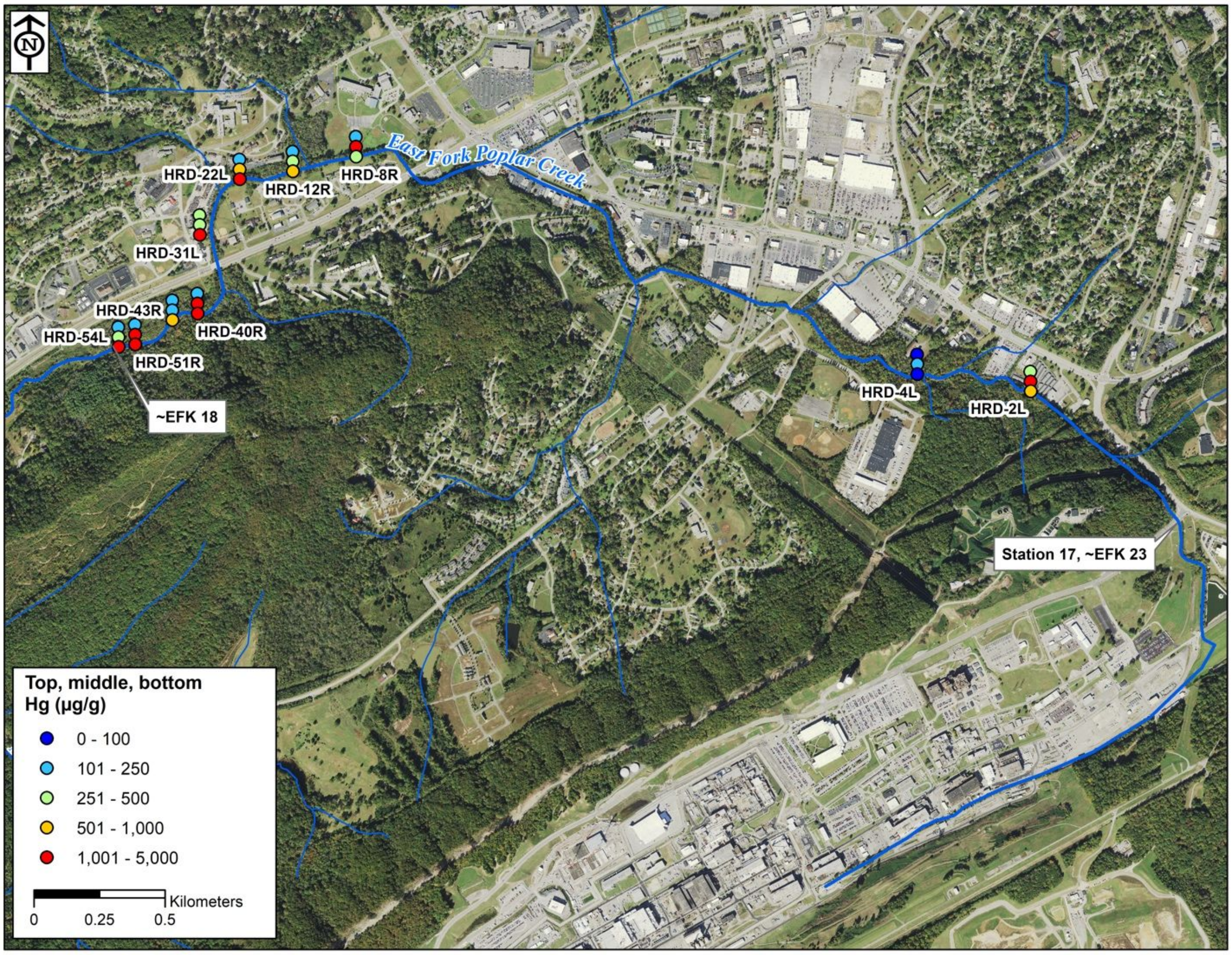

Fig. 1. Map of East Fork Poplar Creek (EFPC) depicting soil sampling locations from the historical release deposits (labeled "HRD") and corresponding Hg concentrations for samples from three depths (top, middle, bottom) at that location. Samples were collected 18 to 23 kilometers (EFK) upstream of the mouth of EFPC. This data was originally presented in Supplementary Information of Dickson et al.,[15], but using "BL" for sample notation instead of "HRD".

2. Methods

2.1. Site Description and Sample Collection

EFPC is a 26-km, low-gradient, low-order stream that originates in the Oak Ridge Reservation in Eastern Tennessee (**Fig. 1**).[15] In total, EFPC drains a 77-km^2 watershed, with groundwater, stormwater runoff, and process and cooling water from the Y-12 NSC contributing to the EFPC flow.[13, 47] The Y-12 NSC is located at the headwaters of the EFPC; from there, the creek extends 3 km until it reaches the boundary of the Oak Ridge Reservation. The creek then travels an additional 23 km through commercial, residential, open-land, and forested areas until its confluence with Poplar Creek. This 23 km reach downstream is referred as "Lower EFPC." Sites in Lower EFPC are designated by the notation "EFK" (East Fork Kilometer), followed by an integer corresponding to the approximate kilometers from the site to the confluence with Poplar Creek. For example, EFK 23 would be the sampling site immediately outside the Y-12 NSC boundary.

This study focused on a subset of samples from a previously identified SB zone of higher Hg concentrations associated with fine-grained coal fines that were deposited during the period of active Hg use at the Y-12 NSC.[15, 16, 41] As such, these dark-colored layers that appear along the exposed bank of the incised stream are referred to as historical release deposits (HRDs), and are typically located 5 to 120 cm below ground surface (Supplementary Information Fig. SI1). In July 2015, 2.5-cm diameter and depth core samples of the HRD were collected from the bank at 70 locations along the stream corridor. The soil samples were immediately placed on dry ice and transferred to −80°C storage at Oak Ridge National Laboratory within 8 h after collection. Samples were subsequently analyzed for major elements (Al, Si, Fe, Ca, Mg, K, Na, Li, Fe, Mn, Ti, P), Hg, MeHg, and physiochemical properties. The SB soils were classified as a loam and silty loam[41] and consist of 1.0% ± 3.8% gravel (mean ± standard deviation), 35.2% ± 14.2% sand, 45.2% ± 10.5% silt, and 18.6% ± 7.7% clay with a mean total carbon content of 1.73% ± 0.86%, mean organic carbon content of 1.41% ± 0.71%, mean nitrogen content of 0.12% ± 0.05%, and a soil pH of 7.4 ± 0.4.[15] In this study, a subset of the HRD samples from 10 of the 70 locations evaluated by Dickson et al.

[15] were selected because of their high Hg content for further characterization using the methods described below. For comparison of elemental content, additional samples were collected from non-contaminated SB zones downstream of the HRD.

2.2. Elemental Analysis

Major elements (Al, Si, Fe, Ca, Mg, K, Na, Li, Fe, Mn, Ti, P) and Hg in these samples were previously reported by Dickson et al.[15]. Sulfur sequential extraction was performed on several samples to extract various oxidation states of sulfur (SO_4^{2-}, S^0, S^-, S^{2-}) and was followed by sulfur isotope composition ($\delta^{34}S$) measurements.[48-50] Method details can be found in the Supplementary Information.

2.3. Scanning Electron Microscopy and Energy Dispersive Spectroscopy

Scanning electron microscopy (SEM) measurements with energy-dispersive spectroscopy (EDS) mapping were performed with a Hitachi S4800 field-emission gun SEM with a backscatter electron detector and a Bruker EDS detector. Prior to analysis, 14 dried EFPC bank soils samples were embedded in an epoxy resin (Buehler vacuum epoxy) and polished to obtain cross-sectional interfaces. The polished samples were then carbon-coated using a Cressington 208 sputter coater. The SEM backscatter electron detector was used to search for Hg-enriched particles. All SEM measurements were performed at 20 keV with brightness turned down and contrast increased relative to normal SEM usage, making it easier to detect brighter, high-Z elements, such as Hg, in the bank soil samples. Once a bright particle was located, a point EDS spectrum was taken at the bright spot to confirm the presence of Hg at that specific location. After receiving confirmation of the presence of Hg from the spot EDS spectrum, a full EDS map was obtained. The EDS map was reanalyzed with a ZAF correction with respect to atomic percent for post-processing. Post-processing of the EDS data, as well as particle and cluster size analysis, was performed with NIH ImageJ.[51, 52] The separate elemental EDS maps were stacked and a line profile was taken across the Hg particle. For the particle and cluster size analysis, a minimum of four individual measurements per particle or cluster were performed. All EDS measurements reported were considered semi-quantitative. Spectrum alignment was performed using an EDS Al+Cu calibration standard and the AlKα and CuKα peak positions. No other standards were used to perform the EDS analyses.

2.4. Transmission electron microscopy and selected area electron diffraction (TEM-SAED)

Focused Ion Beam (FIB) lamella of Hg-enriched HRD soils were prepared by lift-out techniques from the epoxy resin cross-sectional polished SEM samples using a Hitachi NB5000 dual-beam FIB-SEM. The polished samples were coated with a thick layer of carbon. A 3 mm wide by approximately 15 mm long tungsten cap was deposited on the cross-sectional edge. After lift-out, the samples were mounted on an Omniprobe lift-out transmission electron microscopy (TEM) grid and further thinned using a gallium ion beam.

Scanning TEM (STEM) imaging (bright-field and dark-field) and EDS mapping were performed using a Hitachi HF3300 cold field emission S/TEM at an accelerating voltage of 300 keV equipped with a Bruker XFlash EDS silicon drift detector. The HF3300 is also equipped with a secondary electron detector, which allowed for the acquisition of simultaneous SEM and dark-field STEM images. The atomic weight percentages contained in EDS images were calculated using the P/B–ZAF method with Bruker's Esprit 2.0 software. Copper was used for the energy position calibration. A TEM background was used with background points picked using the interactive data fit option. A series fit was chosen for the peak deconvolution method. A tile size of 2 × 2 pixels was chosen for peak deconvolution, resulting in a 512 × 384 pixel image for each elemental EDS map. Selected-area electron diffraction (SAED) measurements were also performed on regions of the FIB lamella. The camera length used to collect the SAED images were calibrated against an aluminum diffraction standard obtained from Ted Pella, Inc.

Based on this measurement, the current instrument calibration had less than 1% error compared with the aluminum standard d-spacings, so calibration corrections to the SAED were not performed.

For comparisons, TEM analysis was also performed on chemically synthesized HgS and a biogenic HgS (bio-HgS) extracellularly synthesized using the sulfate-reducing bacteria *Desulfovibrio desulfuricans* ND132. Details of the synthesis and media are described in the Supplementary Information Section 1. Briefly, abiotic HgS nanoparticles were synthesized by mixing 1 mM Na_2S and 0.05 mM $HgCl_2$ in autoclaved, anoxic deionized water. Bio-HgS nanoparticles were prepared first by incubating ND132 cells in a phosphate-buffered saline (PBS) in the presence of 20 mM Na_2SO_4 and 40 mM pyruvate for 3 days,[53-55] at which sulfate was mostly reduced to sulfide with a measured sulfide concentration of ~20 mM. The culture medium was then taken and mixed with 0.05 mM $HgCl_2$ to form HgS precipitates. Both the biogenic and abiotic HgS precipitates were then vacuum filtered and rinsed with autoclaved, anoxic deionized water before TEM imaging.

2.5. Extended X-ray Absorption Fine-Structure Spectroscopy

The local bonding environment of the Hg in the SB HRD samples was evaluated by Hg L_{III}-edge extended X-ray absorption fine-structure spectroscopy (EXAFS). The EXAFS was collected on beamline 11-2 at the Stanford Synchrotron Radiation Lightsource under dedicated conditions (3 GeV, 500 mA) using an unfocused beam. The beamline was configured with a rhodium mirror, a channel-cut Si(220) phi = 90° monochromator (beam size = 1 mm vertical × 10 mm horizontal), and a 100-element Ge detector. The energy scale was calibrated to the derivative maxima (11,919 eV) of an Au metal foil for Hg. Multiple scans (from 2 to 6) were collected for each sample as they were held at 77 K in a liquid nitrogen cryostat. EXAFS spectra were collected out to $k = 12$ Å^{-1} at a 0.05 Å^{-1} step. Backgrounds were removed from EXAFS spectra using a cubic spline fit with nodes defined by the AUTOBKG function in IFEFFIT. Fourier transformations of k^3-weighted spectra [$k^3*\chi(k)$] were taken across a k range of 3 to 12.7 $Å^{-1}$ using a Kaiser-Bessel window with a 0.5 $Å^{-1}$ sill width.[56]

Spectra were qualitatively compared with previously described spectra for the following 9 Hg compounds: mercury oxide (HgO)[57], Schuetteite[57] ($Hg_3(SO_4)O_2$), cinnabar[57] (α-HgS), metacinnabar[57] (β-HgS), Hg-tetrathiolate[57] (H_2Cyst:Hg = 15), Hg-cysteine[57] (H_2Cyst:Hg = 2.2), Hg-glutathione[57] (GSH:Hg = 2.2), and freshly precipitated nano-HgS aged for 8 days[58]. Additionally, EXAFS spectra were modeled using the Artemis module of Demeter[56] to fit parameters for interatomic distance (ΔR), coordination number (N), and mean-square displacement of interatomic distance (σ^2) across a R range in the Fourier transform from 1.5 to 5 Å. The amplitude reduction factor (S_0^2) was fixed at 0.73.[58] EXAFS fits utilized paths generated in Artemis from structural models of metacinnabar available as a .cif file from the American Mineralogist Crystal Structure Database.[59, 60]

2.6. Metagenomic Sequencing and Analysis

A soil sample from the SB HRD layer at EFK 18.2 (36.00438 N, 84.28246 W) was collected in sterile collection bags (Nasco, Madison, WI, USA), sealed and then stored at −20°C until further processing. DNA was isolated from 1 g of soil using a MO BIO PowerSoil DNA Isolation Kit (QIAGEN Inc., Germantown, MD, USA) following the manufacturer's instructions. The purity and concentration of the extracted DNA was evaluated using a NanoDrop 2000c UV−vis spectrophotometer (Thermo Fisher Scientific, Wilmington, DE, USA). The isolated DNA was stored at −20°C prior to analysis. Shotgun metagenome libraries were constructed by barcoding the extracted DNA by sample and sequenced on the Illumina NextSeq platform with 150 bps paired-end multiplex sequencing (CosmosID Inc., Rockville, MD, USA). Raw sequence reads were binned by barcode and analyzed using the Meta-Genome Rapid Annotation with Subsystem Technology (MG-RAST) server.[61] The MG-RAST analysis pipeline performs quality control, protein prediction, clustering and similarity-based annotation of large metagenomic data sets. Taxa were assigned within the MG-RAST pipeline using a nucleic-acid similarity search. Briefly, representative hits clustered at 97% identity were matched using BLAT (65% identity, e-value cutoff of 10^{-5}) to the M5rna database, which integrates the SILVA, Greengenes and RDP rRNA databases.[62, 63] The relative abundance of taxa refers to the proportion of sequences assigned to each taxonomic hierarchy relative to the total number of taxonomic assignments.

3. Results and Discussion

3.1 Elemental Contents of Bank Core Samples

Average Hg contents in the SB HRD samples were 727 ± 338 mg/kg, greatly exceeding the 8.31 ± 7.98 mg/kg Hg contents reported for non-HRD soils along EFPC[34] (**Table 1**). However, these observed Hg levels are not surprising given the extensive contamination of the site, and they agree with previously reported observations for the HRD layer.[14, 40] Hg contents in the EFPC SB soils have been shown to exceed levels in floodplain soils and streambed sediments in the area (Fig. S2).[6, 14, 32-34, 40, 64]

The average sulfur (S) content of the SB soils was 900 ± 430 mg/kg (**Table 1**), which is comparable to the average soil S content in the US of approximately 1200 mg/kg.[65] For all samples except HRD-43R, the chromium reducible sulfide fraction (we refer as S^- or disulfide) was on average 61% ± 16% of total sulfur and the predominant form of sulfur in the soil samples (**Table 1**). Sulfate (24.9% ± 15.6%) and monosulfide (14.1% ± 4.1%) were other major forms of sulfur. The presence of reduced sulfur is often associated with dissimilatory sulfate-reducing microorganisms (SRMs), and is responsible for biogenic HgS nucleation.[66] It is important to point out that the measured sulfate in HRD samples represent the bulk of any acid-soluble minerals present and pore-water sulfate adsorbed to surfaces or present as a soluble salt formed after drying the samples prior to performing the sequential extractions. Given that the sulfate minerals were not detected by SEM, the measured sulfate contents are likely representative of the pore-water sulfate that was present in the studied samples at the time of sampling.

Despite the relatively average S soil concentrations, the molar ratio of S to Hg was on average 9.04 ± 4.87, indicating a surplus of S relative to Hg, which is needed for HgS formation. However, these ratios are not a definite indication of HgS formation, as S and Hg can exist independently of each other through complexation with other elements in the soil. Therefore, other methods were explored to further probe these associations.

Table 1. Bank soil samples elemental composition from the historical release deposit (HRD) and non-contaminated streambanks (SB) along East Fork Poplar Creek (EFPC). East Fork Kilometer (EFK) represents the distance from the mouth of EFPC to the sample site. Portions of this data was originally presented in Supplementary Information of Dickson et al.,[15], but using "BL" for sample notation instead of "HRD."

Sample ID	**EFK**	**Hg** (mg/kg)	**Al** (g/kg)	**Si** (g/kg)	**Ca** (g/kg)	**Fe** (g/kg)	**TOC** (g/kg)	**S^0** (mg/kg)	**Sulfate** (%)	**Sulfate $\delta^{34}S$ – CDT [‰]**	**Disulfide S^-** (%)	**Disulfide $\delta^{34}S$ – CDT [‰]**	**Monosulfide S^{2-}** (%)	**Monosulfide $\delta^{34}S$ – CDT [‰]**
HRD-2L	22.46	1,143	61.7	287	23.7	32.5	13	500	3.60	ND	76.8	2.3	19.6	1.8
HRD-4L	21.98	147.0	56.0	327	5.30	27.9	12	200	15.3	1.7	75.9	5.2	8.80	2.5
HRD-8R	19.39	522.8	65.7	288	12.9	43.0	21	1,200	17.9	3.1	72.5	ND	9.70	1.3
HRD-12R	19.16	390.2	61.4	292	10.3	36.2	29	800	NA[1]	NA	NA	NA	NA	NA
HRD-22L	18.94	881.5	66.8	271	5.40	47.7	30	1,700	21.5	1.9	65.1	ND	13.4	3.6
HRD-31L	18.66	796.0	74.9	250	9.80	44.4	37	700	NA	NA	NA	NA	NA	NA
HRD-40R	18.31	858.2	65.6	285	6.60	40.1	24	800	NA	NA	NA	NA	NA	NA
HRD-43R	18.20	427.9	71.5	233	9.00	34.9	42	1,200	52.2	2.1	32.8	ND	14.9	6.3
HRD-51R	18.03	1,139	76.7	243	14.8	42.3	39	1,200	30.2	0.9	50.9	ND	18.9	-0.1
HRD-54L	17.97	967.2	75.8	267	8.50	42.4	29	700	33.8	0.4	53.0	ND	13.2	1.4
SB1-7	22.30	18.38	44.1	342	7.3	21.7	9.0	100	NA	NA	NA	NA	NA	NA
SB6-3	18.10	4.01	60.1	323	6.3	31	5.0	600	NA	NA	NA	NA	NA	NA
SB9-5	14.70	0.2	41.5	371	2.3	21.7	4.9	ND	NA	NA	NA	NA	NA	NA
SB15-6	8.80	10.65	38	345	3.2	19.7	22	400	NA	NA	NA	NA	NA	NA

[1]NA = data not available; [2]ND = non-detectable level.

3.3 Mercury-Sulfur Associations

SEM-EDS analysis on HRD-2L and HRD-54L showed multiple spots with overlapping EDS signals at the Hg L-edge and S K-edge, indicating collocation of Hg and S (**Fig. 2**, **Fig. 3**, and **Fig. SI5-SI10**). For all HRD samples SEM imaging indicated HgS clusters (i.e., particle aggregates) ranging from 0.20 to 4.0 µm and containing multiple nano-sized particles (**Fig. SI3, SI4**). No HgS clusters were observed in the SB samples except in one location in sample SB6-3. Particles with collocated Hg and S in sample HRD-2L ranged from 70 to 200 nm in diameter. Particles containing Hg and S in the HRD-54L sample were larger, ranging from 520 to 4450 nm in diameter. These SEM-EDS data indicate Hg-S association, which could occur in various forms including HgS mineral particles, Hg bound to thiol groups or disulfide in SOM[67, 68], and other mineral particles (e.g. aluminum and iron (hydr)oxides[69, 70], clays[69, 71], or other metal sulfide particles[72]) that host both Hg and S (**Fig. 3, SI5-SI10**). For example, in one sample from HRD-54L, we observed in the spatially resolved EDS spectra increased signal intensity at energies corresponding to the Hg L-edge, S K-edge, as well as the Ca, Si, and Al K-edges (**Fig. 3**). Increased signal from all of these elements on the HRD-54L sample suggests the presence of an Al- and Si-bearing particle that hosts HgS co-precipitate or crust. Alternatively, the Hg could be bound to organic S ligands that are components of soil organic compounds that coat Al-bearing mineral particles.[73]

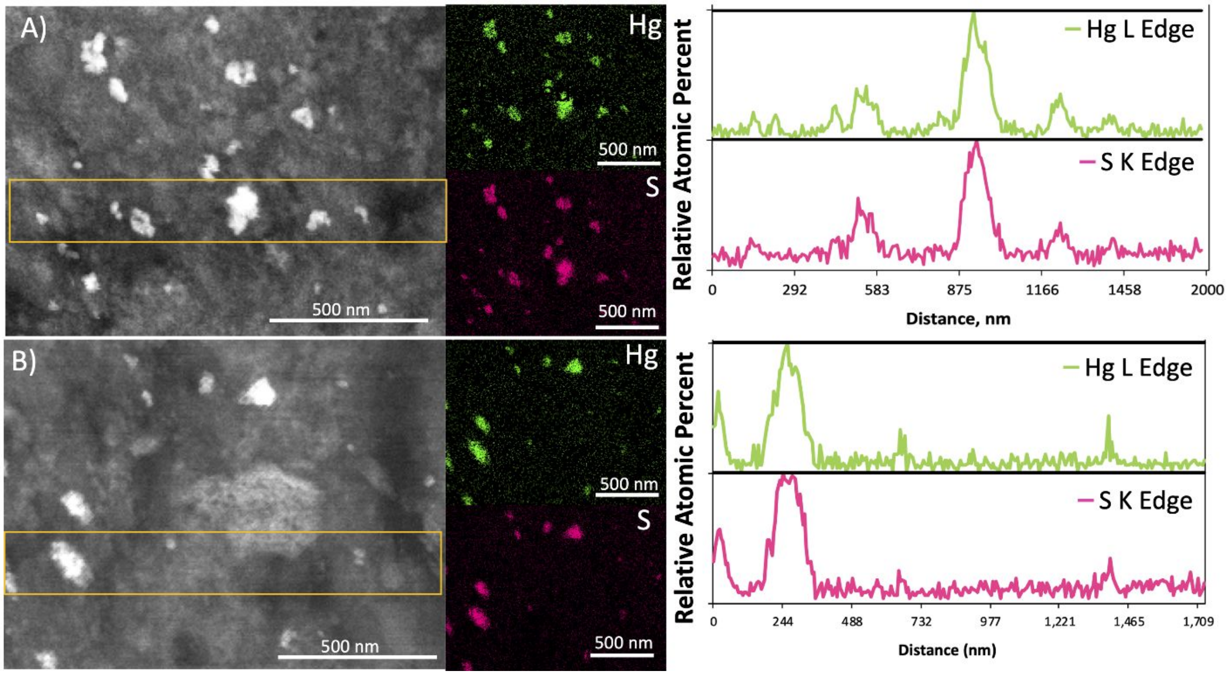

Fig. 2. Backscattered-electron SEM imaging (left) and corresponding EDS average horizontal line profiles for Hg and S (right) for streambank soil HRD-2L Map 1 (A) and Map 2 (B).

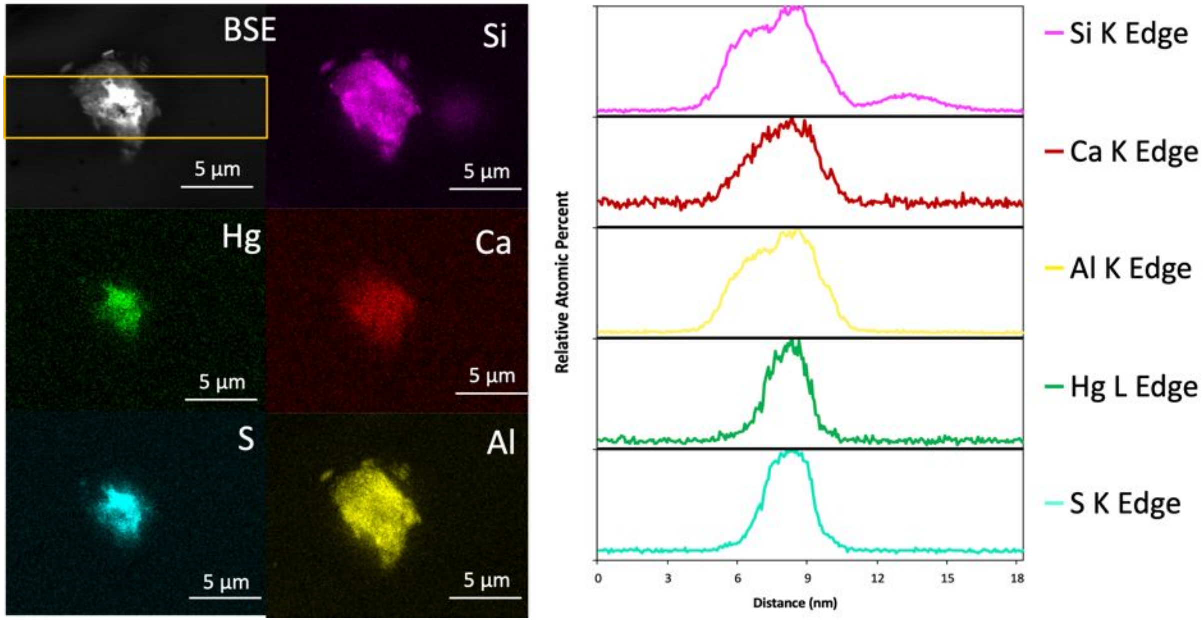

Fig. 3. Left: Backscattered-electron SEM for streambank soil HRD-54L Map 1 showing the presence of Si, Ca, Al, Hg, and S. **Right**: Corresponding EDS average horizontal line profiles for each element.

3.3 Crystallography and Local Binding Environment

The analysis of a subset of the streambank soils (n=3) by Hg L_3-edge EXAFS revealed that the local coordination state of Hg resembled nanocrystalline HgS (nano-HgS). The k^3-weighted EXAFS data for all samples shared similar spectral features at k = 3-7 $Å^{-1}$, with subtle differences in intensities at k = 9-12 $Å^{-1}$ (**Fig. 4**). Interestingly, while HRD-2L and HRD-51L contained similar Hg content (~1100-1200 mg/kg; **Table 1**), the spectral features of HRD-51L were of lesser intensity in both the Fourier transforms and the k^3-weighted data.

Shell-by-shell fitting of EXAFS spectra for the streambank soils indicated that the average characteristic interatomic distance of nearest neighbor atoms was ~2.54 Å, indicating Hg coordination state similar to both β-HgS and freshly precipitated nano-HgS (**Table 2**, **Table SI1**). This first-shell Hg peak is also distinctly different from characteristic interatomic distances for other possible reference materials, including Hg-SOM (**Table SI1**). However, the k^3-weighted EXAFS spectra for the streambank soils shared key features with spectra of the fresh nano-HgS, particularly with the doublet peaks at around 4.75 $Å^{-1}$ and 10.8 $Å^{-1}$ (**Fig. 4**, dashed lines A and B). These features were not observed in the β-HgS spectra. Despite accounting for most factors in the EXAFS fits (R factor < 0.10), coordination numbers of near-neighbor atoms (i.e., Hg-S and Hg-Hg back-scattering atoms) were lower than the corresponding values for reference nano-HgS and β-HgS. While we observed differences in spectral intensity for HRD-2L and HRD-51L samples, the fitting parameters from the shell-by-shell models (i.e. coordination numbers in Table 2) did not reveal observable differences between soil samples. Regardless, the shell-by-shell fitting results of EXAFS spectra for all 3 soils suggest significantly fewer S and Hg near-neighbor back-scattering atoms for Hg species in the streambank soils compared to the β-HgS crystal lattice (**Table 2**).

The appearance of undercoordinated Hg in a HgS structure could be due to several reasons. First, undercoordination can be caused by artefacts of the spectra, such as saturation of the detector (deadtime) with sample X-rays, resulting in reduced signal that led to underestimation of Hg-S coordination number. However, EXAFS fits for samples remained unchanged after correcting for deadtime; thus, we believe detector saturation was minimal. More likely, the appearance of undercoordinated Hg in a HgS structure suggests that Hg is predominantly in the form of aggregated nanoparticles of HgS. The apparent coordination number for nanoscale crystals will be less than that observed in larger mineral forms because of the high specific surface area of nanometer-scale (<10 nm) crystals and the larger portion of atoms that comprise the crystal lattice edge.[74-76] Based on the coordination results shown in Table 2, we estimated (using crystallite modeling methods described in prior studies[77, 78]) that the HgS clusters were ~1 nm in diameter (**see Figure SI11**). The nanocrystalline features of the HgS particles has implications for the reactivity of these particles. In order to confirm this phenomenon, the sample HRD-2L was further analyzed by TEM-SAED as a means to evaluate size, crystallinity, and morphology of the nanoparticulate HgS.

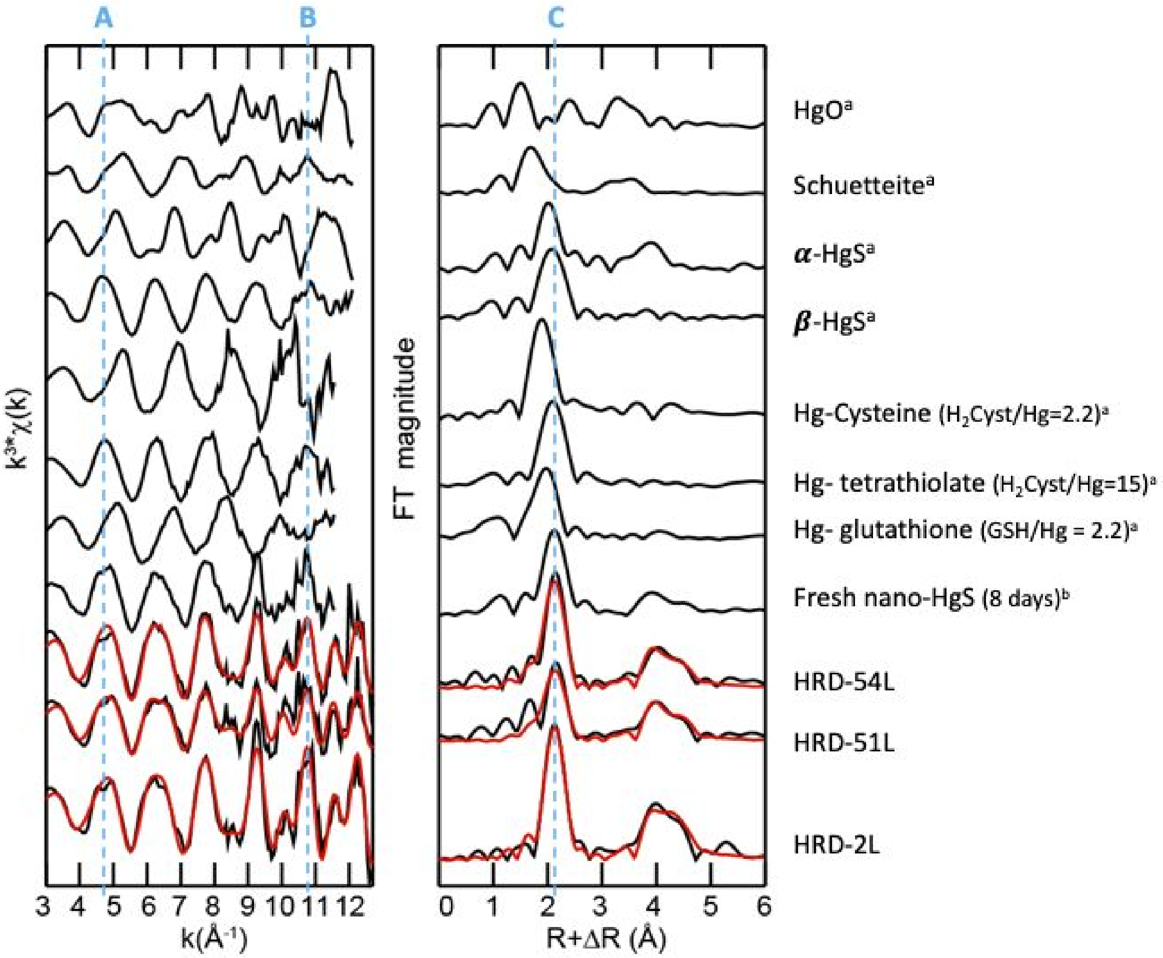

Fig. 4. Normalized bulk Hg-EXAFS spectra and Fourier transforms of streambank soil samples HRD-2L, HRD-54L, and HRD-51L. Spectra are compared with published data for other possible Hg complexes in this environment: [a] Avellan et al.[57]; [b]Pham et al.[58]. Solid line-experimental data; solid red line- nonlinear least-squares fits; vertical blue line- visual guide. Numerical results presented in **Table 2**.

Table 2. Parameters for shell-by-shell interatomic fits of EXAFS spectra for historical release deposit (HRD) streambank samples compared to expected values for fully coordinated metacinnabar (β-HgS). A-B is the absorber-backscatter atom pair. Adjustable parameters include coordination number (N), bond distances (R), mean square atomic displacement (σ^2), and the change in threshold energy (ΔE_0). The threshold energy (E_0) was set at 12,285 eV. The amplitude reduction factor (S_0^2) was fixed at 0.73 based on fitting of the β-HgS [58].

Sample	A-B	N	R(Å)	σ^2	ΔE	R factor[B]
HRD-54L	Hg-S	4.5 ±0.5	2.53 ±0.01	0.0063 ±0.0013[A]	7.2 ±1.4	0.045
	Hg-Hg	4.7 ±3.0	4.14 ±0.01	0.0037 ±0.0032		
	Hg-S	4.9 ±2.5	4.81 ±0.03	0.0063 ±0.0013[A]		
HRD-51L	Hg-S	3.8 ±0.5	2.54 ±0.01	0.0085 ±0.0019[A]	9.0 ±2.0	0.055
	Hg-Hg	5.2 ±2.5	4.17 ±0.01	0.0043 ±0.0025		
	Hg-S	6.5 ±2.4	4.83 ±0.02	0.0085 ±0.0019[A]		
HRD-2L	Hg-S	3.7 ±0.4	2.53 ±0.00	0.0030 ±0.0009[A]	6.3 ±1.0	0.035
	Hg-Hg	6.0 ±3.0	4.15 ±0.01	0.0038 ±0.0026		
	Hg-S	4.4 ±1.8	4.84 ±0.02	0.0030 ±0.0009[A]		
β-HgS (model compound)[58]	Hg-S	4	2.53	0.003	2.5	
	Hg-Hg	12	4.15	0.006		
	Hg-S	12	4.83	0.009		

[A] Paths were linked in the fitting;

[B] $$R-factor = \frac{\sum_i^{Nfit}(\chi_i^{measured} - \chi_i^{model}(x))^2}{\sum_i^{Nfit}(\chi_i^{measured})^2}$$

TEM-SAED analysis of the HRD-2L samples indicated clusters of defect-containing HgS nanoparticles (**Fig. 5**, **Fig. 6**). Brightfield TEM images of HRD-2L indicate aggregates of spherical crystalline nanoparticles each about 10 nm in diameter (**Fig. 5B, C, F, G**). Lattice fringe patterns were observed in only a subset of nanoparticles, which is expected because the random arrangement of the particles prevented the orientation required for Bragg diffraction of the electron beam. Nanoparticles near the edge of the particle aggregates were focused on for clarity and to avoid Moire interference patterns of the lattice fringes of overlapping nanoparticles. The HRTEM images were fast Fourier transformed (FFT) to show the lattice spacings of the nanocrystals. For the most part, lattice spaces are consistent with the metacinnabar polymorph of HgS viewed down the [-233] and [0-11] zone axes (**Fig. 6**). The striped and chevron patterns in some of the HRTEM lattice fringe images are indications of crystallographic defects such as stacking faults and twin boundaries in the nanoparticles. This is further reflected by the slight deviation in d-spacing for the [200] plane looking down the [0-11] zone axis (**Fig. 6B**). These crystallographic defects can lead to nanoparticles with higher surface energies, thus potentially increasing their reactivity and dissolution behaviors relative to particles lacking such defects.[79] While SAED spectra are, for the most part, indicative of β-HgS, the observed distortion at index [200] supports the low coordination number modeled by the EXAFS fits.[80]

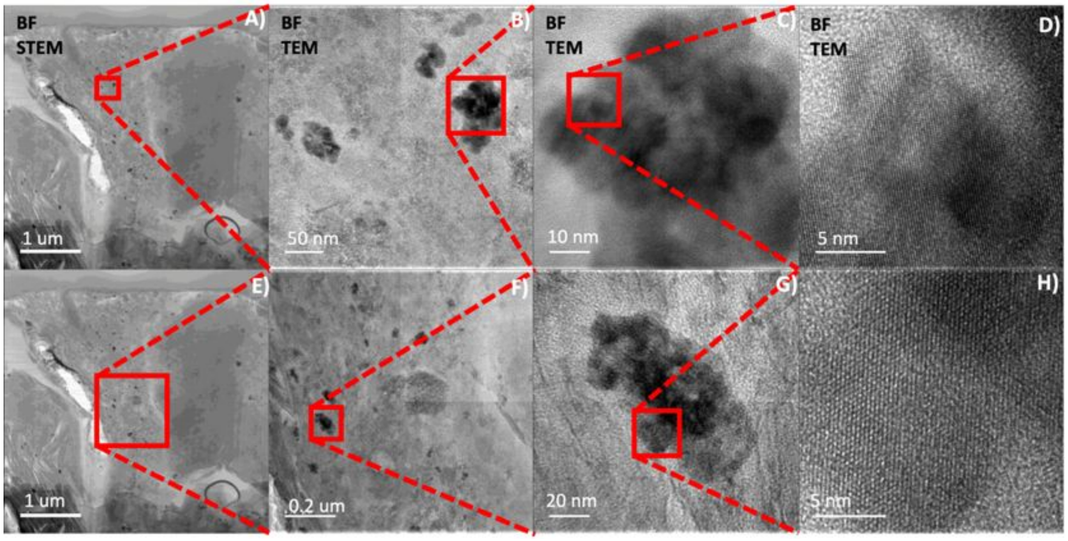

Fig. 5. Bright field TEM images of FIB liftout from HRD-2L streambank soil sample (A and E). The FIB liftout was collected from the cluster of particles shown in Fig. SI4. Magnification increases from left to right (B-D and F-H) and is centered on the area delineated with red box.

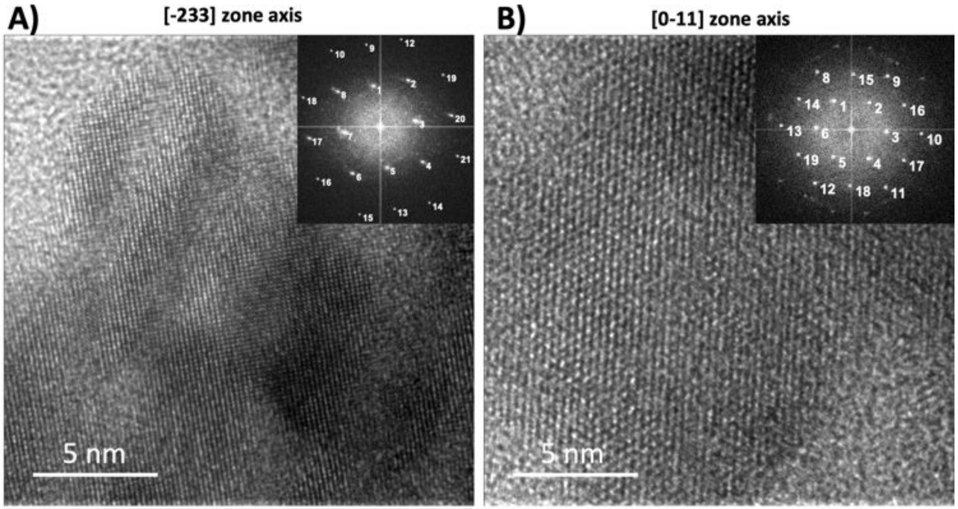

Spot#	Miller Index	d-Spacing (nm)	Lit. d-Spacing (nm)
1	311	0.173	0.177
2	3-13	0.132	0.134
3	0-22	0.195	0.207
4	-3-31	0.129	0.134
5	-3-1-1	0.172	0.177
6	-31-3	0.132	0.134

Spot#	Miller Index	d-Spacing (nm)	Lit. d-Spacing (nm)
1	-111	0.331	0.338
2	111	0.340	0.338
3	200	0.314	0.293
4	1-1-1	0.328	0.338
5	-1-1-1	0.341	0.338
6	-200	0.316	0.293

Fig. 6. HRTEM and corresponding SAED pattern for a FIB liftout from streambank soil HRD-2L.

The imaging of HRD-2L was further compared to the TEM-SAED of a biogenic HgS sample synthesized in the lab (**Fig. 7**). In both figures we observe similar structural defects in the form of twinning, stacking faults, and dislocation. These defects may be attributed to biogenic polymers adsorbing to the nanoparticle surface, stabilizing the nanoparticle, retarding nucleation and allowing more flexibility in the assembly of particles.[79, 81-83]

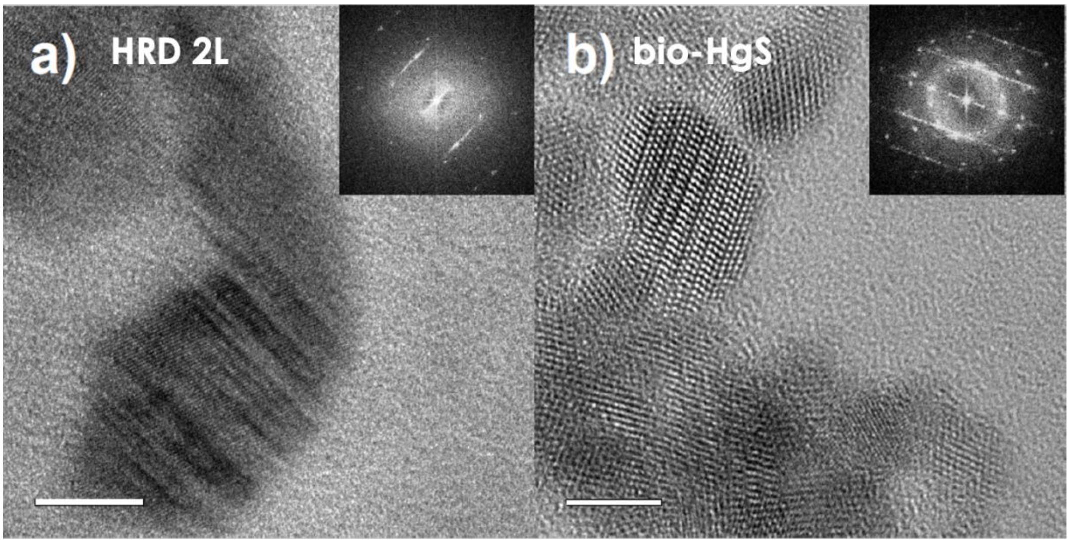

Fig. 7. TEM images and corresponding SAED patterns of A) streambank soil from EFPC, and B) biogenic HgS synthesized in the lab.

3.4 Pathways of Formation

The combined observations from SEM-EDS, EXAFS, and TEM suggest poorly ordered HgS nanoparticles in streambank samples from EFPC. The mechanism of this HgS formation is relevant for transformations of soluble Hg species that are continuously supplied to the riparian corridor from upland areas. Insights on theses transformations and modes of occurrence of Hg in the stream are needed to guide management of the site. The traditional paradigm suggests that HgS formation is of biogenic nature, in which Hg(II) reacts with sulfide ions produced by SRMs in anaerobic environments. However, recent research has also identified an abiogenic chemical or photochemical HgS formation pathway via dealkylation of Hg-thiolate complexes in SOM and polymerization of HgS.[66, 84, 85] Given the oxygenated nature of the upland floodplain soils of the EFPC catchment, a previous study[36] argues that this abiogenic pathway explains the presence HgS nanoclusters.

For the streambank soils that are the focus of our study, the aforementioned abiotic pathways is a potential mechanism of nanocrytalline HgS formation; however, this process is kinetically unfavorable. Instead, the traditional mode of biogenic sulfide formation may be occurring in these soils, even though they are exposed to oxygenated conditions. In our metagenomic analysis of the SB HRD soils (Fig. 8), we observed SRMs that are prevalent in bacterial (Deltaproteobacteria, Thermodesulfovibrio(Nitrospirae), Firmicutes, Thermodesulfobacteria) and archaeal lineages (Euryarchaeota, Crenarchaeota).[86] At the family level, 18 clades represent most of the known SRMs in environmental samples (**Table SI2**). The relative abundance of these clades in the EFPC HRD soil metagenome is shown in **Fig. 8**; additional details on taxa abundance can be found in the Supplementary Information (SI Section 4). At the family level, the Desulfovibrionaceae were the most abundant SRM (0.59%), followed by the Syntrophobacteraceae (0.35%), the Peptococcaceae (0.33%) and the Desulfobacteraceae (0.32%). The total relative abundance for all identified SRM was 2.49%.

The results demonstrate that a diverse group of SRMs are present in the microbial community of EFPC HRD soils. Therefore, dissimilatory sulfate reduction may represent a significant source of biogenic sulfide in these soils. Frequent flooding of streambank soils combined with detection of both reduced S and SRMs therefore argues that biogenic HgS nanocluster formation is a relevant mechanism of HgS formation. It is noteworthy that the measured δ^{34}S values of chromium-reducable sulfides were higher (-0.1 to +6.3 ‰) than typically found in biogenic sulfides formed as a result of SRMs (< -10 ‰)[87]. However, these values are similar to the ranges of δ^{34}S measured in the acid-soluble sulfate found in the studied soils (+0.4 to +3.1 ‰) and dissolved sulfate in local surface waters (+2.7 to +5.8 ‰)[88]. This suggest that SRMs occurs under sulfate-depleted conditions leading to insignificant S isotope fractionations because of complete reduction of porewater sulfate to sulfides such as HgS particles. The concentration of dissolved sulfate in local surface waters are relatively low (average 0.13 mM)[88], thus any of this sulfate contributed to the studied soils during flooding events would be quickly metabolized (reduced to sulfide) by SRMs.

The structural defects of nanocrystalline HgS in TEM analysis of streambank soil HgS particles are similar to defects observed for biological-HgS nanoparticles produced in the laboratory. These defects are likely due to polymers that are present during HgS nucleation. For example, structural defects, such as those observed in the synthetic bio-HgS, may occur if Hg^{2+} complexes with biologically produced sulfide in the extracellular polymeric substance (EPS) rich environment outside of the SRM cell envelope.[79, 81-83] Similarly for HgS nanoparticles produced by abiotic dealkylation of Hg-thiolate moities, NOM in soils may affect nano-HgS formation, growth, aggregation, and dissolution reactions[67, 89-91] that alter lattice structure.[92] However, the dealkylation of Hg-thiolate complexes is significantly slower than the complexation of Hg^{2+} with free sulfides. As such, the abiogenic pathway could be expected to yield less defective HgS structures than those of biogenic origin.[66, 93] Furtherwork is needed to directly compare abiotic delakylation and biogenic proceses for their rates of nanocrstyalline HgS formation as well as the properties of the material products, including crystal lattice structure and particle morphology.

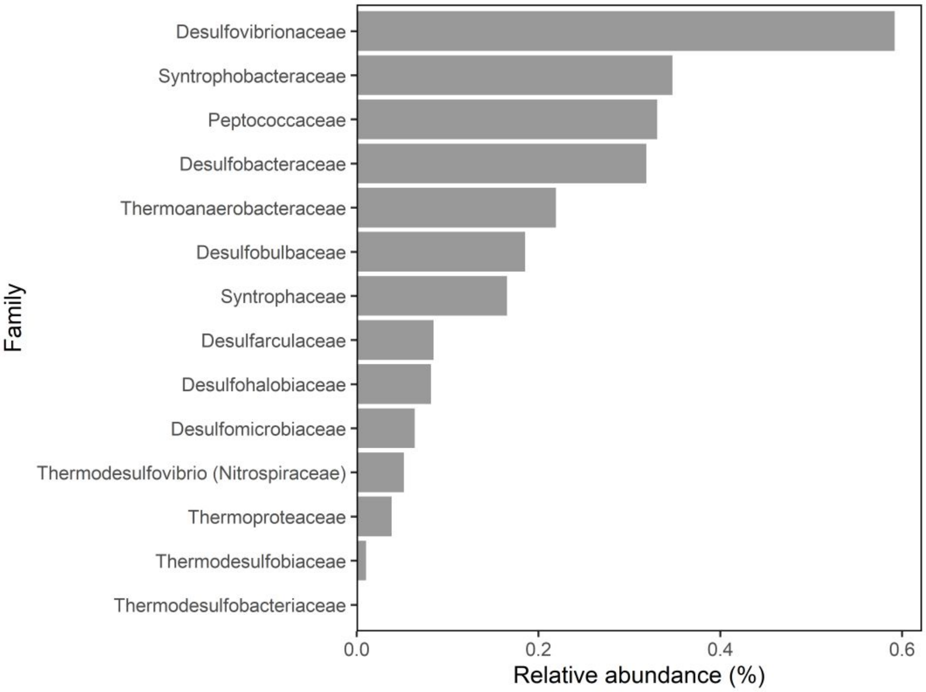

Fig. 8. Distribution of taxa in EFPC HRD soil. Relative abundance of taxa at the family level associated with sulfate reduction.

4. Environmental Implications

In this work, we used a variety of characterization techniques to identify disordered HgS nanoclusters in an exposed streambank soil with moderate S content from EFPC. Because of the observed structural defects in the nanoparticles, the HgS particles were probably formed in the presence of an organic polymer such soil organic matter or the EPS of SRMs. These observations provide further evidence for the persistence of nanocrystalline HgS in oxic soil settings, rather than their presence being limited to anoxic sediments and porewater[23-27] and other settings with high concentrations of available sulfide.[28-30] Furthermore, we observed that HgS particles were co-located with other major elements in soils, indicating that the nanocrystalline HgS are agglomerated or co-precipitated with other host particles.

Our observations in EFPC bank soils may be applicable to other Hg-contaminated fluvial systems that experiences dynamic redox conditions and where bank erosion is a main source of Hg mobilization and transport. Within the US, example systems include waterways downstream of historically contaminated sites, such as textile factories (e.g., South River, VA) and abandoned mines of the "mercury mineral belts"[94] in Alaska[95], California[29, 96], Nevada[97], and Oregon[98, 99]. Additionally, riverbank erosion serves as a long-term Hg input to waterways near active sites of artisanal and small-scale gold mining,[100-102] a mining technique in which large amounts of liquid elemental mercury are added to soils to extract gold.

These results add to the growing literature underlining the importance of studying the nanoscale structure of HgS particles and how it relates to bioavailability. While β-HgS was once viewed as an immobile sink for mercury, research in the last decade has demonstrated nano-HgS, particularly when formed in the presence of DOM, to be more soluble and more bioavailable compared to macrocrystalline metacinnabar.[10, 91, 103, 104] Nanoparticles in general have demonstrated increased reactivity relative to their bulk-scale counterparts, often attributed to unique structure and surface properties.[105-108] For example, sorption and dissolution properties of nanoparticles are dependent on nanocrystal facets and defect structure.[79, 81, 109-113] These phenomena have yet to be confirmed for nano-HgS, but would likely have implications for its reactivity and mobility. Indeed, stable Hg isotope tracing of various fractions of EFPC sediments suggest continuous cycling of Hg between particulate, dissolved and absorption phases in the stream.[114, 115]

The dynamic hydrologic conditions of streambank soils should be considered in their impact on the speciation and resulting structure of Hg in industrially impacted soils. Moreover, frequent flooding and erosion of streambank soils will make nano-HgS very suspectable to mobilization, and the structure of the mobilized HgS will likely further impact its reactivity. During streambank erosion, for example, nano-HgS will be deposited into the stream, where depending on its facets and defect density, may exhibit enhanced solubility, producing more bioavailable Hg(II) complexes. Additionally, bacteria have been observed to preferentially attach to defects on nanocrystalline particles[116], which, in the case of nano-HgS, may result in enhanced adsorption by methylators. Similarly, in flooding events, mercury associated with nano-HgS entrapped in soil may be mobilized via dissolution reactions. In both cases of particle erosion and dissolution, the nanoscale structure of HgS will likely impact the distribution of mercury and the susceptibility of the metal for further transformation. It is therefore necessary to study the microscopic structure of nano-HgS to elucidate implications for environmental reactivity, transport, and bioavailability.

5. Acknowledgements

This research was sponsored by the Office of Biological and Environmental Research within the Office of Science of the U.S. Department of Energy (DOE), as part of the Environmental System Science supported Critical Interfaces Science Focus Area project at the Oak Ridge National Laboratory (ORNL), which is managed by UT-Battelle, LLC under Contract No. DE-AC05-00OR22725 with DOE. The DOE Environmental

System Science program under award DE-SC0019408 also provided partial support. Use of the Stanford Synchrotron Radiation Lightsource, SLAC National Accelerator Laboratory, is support by the DOE Office of Science, Office of Basic Energy Sciences under Contract No. DE-AC02-76SF00515. B.K. Robertson was supported under Minority Serving Institution Program (MSIP) FY2020 grant (RFP No. 0000542525) administered by the DOE Office of Environmental Management. The authors would like to thank Johnbull O. Dickson and Leroy Gomez for providing the streambank image and supporting the collection of the streambank soil samples analyzed in this study. We would also like to thank Tom Greer of ORNL Metrology for prepaing the SEM sample mounts. Faye Koenigsmark and Michelle Chiu was supported by the ORNL Graduate Opportunities program (Task Order 4000150576) and MSIP at ORNL, respectively.

6. Supporting Information

SI Section 1: Methods; Section 2: Elemental Analysis; Section 3: Microscopy and Spectroscopy Analysis; Section 4: Metagenomic Sequencing and Analysis

7. References

(1) Pavlović, P.; Mitrović, M.; Dordević, D.; Sakan, S.; Slobodnik, J.; Liška, I.; Csanyi, B.; Jarić, S.; Kostić, O.; Pavlović, D.; et al. Assessment of the contamination of riparian soil and vegetation by trace metals - a danube river case study. *Science of the Total Environment* **2016**, *540*, 396-409. DOI: 10.1016/j.scitotenv.2015.06.125.

(2) Rice, P. M.; Ray, G. J. Heavy metals in the flood plain deposits along the upper clark fork river. **1972**.

(3) Ye, C.; Li, S.; Zhang, Y.; Zhang, Q. Assessing soil heavy metal pollution in the water-level-fluctuation zone of the three gorges reservoir, china. *Journal of Hazardous Materials* **2011**, *191*, 366-372. DOI: 10.1016/j.jhazmat.2011.04.090.

(4) Grigal, D. Mercury sequestration in forests and peatlands: A review. *J Environ Qual* **2003**, *32*, 393-405.

(5) Obrist, D. Mercury distribution across 14 u.S. Forests. Part ii: Patterns of methyl mercury concentrations and areal mass of total and methyl mercury. *Environmental Science & Technology* **2012**, *46* (11), 5921-5930. DOI: 10.1021/es2045579.

(6) Poulin, B. A.; Aiken, G. R.; Nagy, K. L.; Manceau, A.; Krabbenhoft, D. P.; Ryan, J. N. Mercury transformation and release differs with depth and time in a contaminated riparian soil during simulated flooding. *Geochimica et Cosmochimica Acta* **2016**, *176*, 118-138. DOI: 10.1016/j.gca.2015.12.024.

(7) Weber, F. A.; Voegelin, A.; Kretzschmar, R. Multi-metal contaminant dynamics in temporarily flooded soil under sulfate limitation. *Geochimica et Cosmochimica Acta* **2009**, *73*, 5513-5527. DOI: 10.1016/j.gca.2009.06.011.

(8) Fulda, B.; Voegelin, A.; Ehlert, K.; Kretzschmar, R. Redox transformation, solid phase speciation and solution dynamics of copper during soil reduction and reoxidation as affected by sulfate availability. *Geochimica et Cosmochimica Acta* **2013**, *123*, 385-402. DOI: 10.1016/j.gca.2013.07.017.

(9) Kucharzyk, K. H.; Deshusses, M. A.; Porter, K. A.; Hsu-Kim, H. Relative contributions of mercury bioavailability and microbial growth rate on net methylmercury production by anaerobic mixed cultures. *Environmental Sciences: Processes and Impacts* **2015**, *17*, 1568-1577. DOI: 10.1039/c5em00174a.

(10) Zhang, T.; Kucharzyk, K. H.; Kim, B.; Deshusses, M. A.; Hsu-Kim, H. Net methylation of mercury in estuarine sediment microcosms amended with dissolved, nanoparticulate, and microparticulate mercuric sulfides. *Environmental Science and Technology* **2014**, *48*, 9133-9141. DOI: 10.1021/es500336j.

(11) US-EPA. National priorities list (npl) sites-by state. **2020**.

(12) Hollerman, W.; Holland, L.; Ila, D.; Hensley, J.; Southworth, G.; Klasson, T.; Taylor, P.; Johnston, J.; Turner, R. Results from the low level mercury sorbent test at the oak ridge y-12 plant in tennessee. *Journal of Hazardous Materials* **1999**, *68*, 193-203. DOI: 10.1016/S0304-3894(99)00027-8.

(13) Brooks, S. C.; Southworth, G. R. History of mercury use and environmental contamination at the oak ridge y-12 plant. *Environmental Pollution* **2011**, *159*, 219-228. DOI: 10.1016/j.envpol.2010.09.009.

(14) Southworth, G.; Ketelle, R. Sources of mercury to east fork poplar creek downstream from the y-12 national security complex : Inventories and export rates. *Security* **2010**.

(15) Dickson, J. O.; Mayes, M. A.; Brooks, S. C.; Mehlhorn, T. L.; Lowe, K. A.; Earles, J. K.; Goñez-Rodriguez, L.; Watson, D. B.; Peterson, M. J. Source relationships between streambank soils and streambed sediments in a mercury-contaminated stream. *Journal of Soils and Sediments* **2019**, *19*, 2007-2019. DOI: 10.1007/s11368-018-2183-0.

(16) Southworth, G.; Mathews, T.; Greeley, M.; Peterson, M.; Brooks, S.; Ketelle, D. Sources of mercury in a contaminated stream-implications for the timescale of recovery. *Environmental Toxicology and Chemistry* **2013**, *32*, 764-772. DOI: 10.1002/etc.2115.

(17) Rhoades, E. L.; O'Neal, M. A.; Pizzuto, J. E. Quantifying bank erosion on the south river from 1937 to 2005, and its importance in assessing hg contamination. *Applied Geography* **2009**, *29*, 125-134. DOI: 10.1016/j.apgeog.2008.08.005.

(18) Diringer, S. E.; Berky, A. J.; Marani, M.; Ortiz, E. J.; Karatum, O.; Plata, D. L.; Pan, W. K.; Hsu-Kim, H. Deforestation due to artisanal and small-scale gold mining exacerbates soil and mercury mobilization in madre de dios, peru. *Environmental Science and Technology* **2020**. DOI: 10.1021/acs.est.9b06620.

(19) Gray, J. E.; Hines, M. E.; Higueras, P. L.; Adatto, I.; Lasorsa, B. K. Mercury speciation and microbial transformations in mine wastes, stream sediments, and surface waters at the almadén mining district, spain. *Environmental Science and Technology* **2004**, *38*, 4285-4292. DOI: 10.1021/es040359d.

(20) Roulet, M.; Lucotte, M.; Farella, N.; Serique, G.; Coelho, H.; Sousa Passos, C. J.; De Jesus Da Silva, E.; Scavone De Andrade, P.; Mergler, D.; Guimaraes, J. R. D.; et al. Effects of recent human colonization on the presence of mercury in amazonian ecosystems. *Water, Air, and Soil Pollution* **1999**, *112*, 297-313. DOI: 10.1023/A.

(21) Leigh, D. S. Mercury-tainted overbank sediment from past gold mining in north georgia, USA. *Environmental Geology* **1997**, *30*, 244-251. DOI: 10.1007/s002540050153.

(22) Dai, Z. H.; Feng, X.; Zhang, C.; Shang, L.; Qiu, G. Assessment of mercury erosion by surface water in wanshan mercury mining area. *Environmental Research* **2013**, *125*, 2-11. DOI: 10.1016/j.envres.2013.03.014.

(23) Sunderland, E. M.; Gobas, F. A. P. C.; Branfireun, B. A.; Heyes, A. Environmental controls on the speciation and distribution of mercury in coastal sediments. *Marine Chemistry* **2006**, *102*, 111-123. DOI: 10.1016/j.marchem.2005.09.019.

(24) Moreau, J.; Webb, R.; Banfield, J. F. Ultrastructure, aggregation-state, and crystal growth of biogenic nanocrystalline sphalerite and wurtzite. *American Mineralogist* **2004**, *89*, 950-960.

(25) Lau, B. L. T.; Hsu-Kim, H. Precipitation and growth of zinc sulfide nanoparticles in the presence of thiol-containing natural organic ligands. *Environmental Science and Technology* **2008**, *42*, 7236-7241. DOI: 10.1021/es801360b.

(26) Weber, F. A.; Voegelin, A.; Kaegi, R.; Kretzschmar, R. Contaminant mobilization by metallic copper and metal sulphide colloids in flooded soil. *Nature Geoscience* **2009**, *2*, 267-271. DOI: 10.1038/ngeo476.

(27) Hamilton-Taylor, J.; Davison, W.; Morfett, K. The biogeochemical cycling of zn, cu, fe, mn, and dissolved organic c in a seasonally anoxic lake. *Limnology and Oceanography* **1996**, *41*, 408-418. DOI: 10.4319/lo.1996.41.3.0408.

(28) Merritt, K. A.; Amirbahman, A. Mercury dynamics in sulfide-rich sediments: Geochemical influence on contaminant mobilization within the penobscot river estuary, maine, USA. *Geochimica et Cosmochimica Acta* **2007**, *71*, 929-941. DOI: 10.1016/j.gca.2006.10.012.

(29) O'Day, P. A.; Carroll, S. A.; Randall, S.; Martinelli, R. E.; Anderson, S. L.; Jelinski, J.; Knezovich, J. P. Metal speciation and bioavailability in contaminated estuary sediments, alameda naval air station, california. *Environmental Science and Technology* **2000**, *34*, 3665-3673. DOI: 10.1021/es9913030.

(30) Luther, G. W.; Meyerson, A. L.; Krajeswki, J. J.; Hires, R. Metal sulfides in estuarine sediments. *J. Sediment. Petrol.* **1980**, *50*, 1117-1120. DOI: 10.1306/212f7b94-2b24-11d7-8648000102c1865d.

(31) Howarth, R. W.; Stewart, J. W. B.; Ivanov, M. V. M. V. Sulphur cycling on the continents : Wetlands, terrestrial ecosystems, and associated water bodies. **1992**.

(32) Revis, N. W.; Osborne, T. R.; Holdsworth, G.; Hadden, C. Distribution of mercury species in soil from a mercury-contaminated site. *Water, Air, and Soil Pollution* **1989**, *45*, 105-113. DOI: 10.1007/BF00208581.

(33) Pant, P.; Allen, M.; Tansel, B. Mercury contamination in the riparian zones along the east fork poplar creek at oak ridge. *Ecotoxicology and Environmental Safety* **2011**, *74*, 467-472. DOI: 10.1016/j.ecoenv.2010.10.009.

(34) Han, F. X.; Shiyab, S.; Chen, J.; Su, Y.; Monts, D. L.; Waggoner, C. A.; Matta, F. B. Extractability and bioavailability of mercury from a mercury sulfide contaminated soil in oak ridge, tennessee, USA. *Water, Air, and Soil Pollution* **2008**, *194*, 67-75. DOI: 10.1007/s11270-008-9699-7.

(35) Barnett, M. O.; Harris, L. A.; Turner, R. R.; Stevenson, R. J.; Henson, T. J.; Melton, R. C.; Hoffman, D. P. Formation of mercuric sulfide in soil. *Environmental Science and Technology* **1997**, *31*, 3037-3043. DOI: 10.1021/es960389j.

(36) Manceau, A.; Lemouchi, C.; Enescu, M.; Gaillot, A. C.; Lanson, M.; Magnin, V.; Glatzel, P.; Poulin, B. A.; Ryan, J. N.; Aiken, G. R.; et al. Formation of mercury sulfide from hg(ii)-thiolate complexes in natural organic matter. *Environmental Science and Technology* **2015**, *49*, 9787-9796. DOI: 10.1021/acs.est.5b02522.

(37) Miller, J. J.; Bremer, E.; Curtis, T.; Chanasyk, D. S. An assessment of nutrient dynamics in streambank soils of the lower little bow river in southern alberta using ion exchange membranes. *Water Quality Research Journal of Canada* **2017**, *52*, 196-208. DOI: 10.2166/wqrj.2017.007.

(38) Bohn, C. Biological importance of streambank stability. *Rangelands* **1986**, *8*, 55-56.

(39) Green, D. M.; Kauffman, J. B. Nutrient cycling at the land-water interface: The importance of the riparian zone. *Practical Approaches to Riparian Resource Management: An Education Workshop. US Bureau of Land Management. Billings, MT* **1989**, 61-68.

(40) Watson, D.; Bevelhimer, M.; Brandt, C.; Derolph, C.; Brooks, S.; Mayes, M.; Olsen, T.; Dickson, J.; Peterson, M.; Ketelle, R. Evaluation of lower east fork poplar creek mercury sources–model update. **2016**. DOI: ORNL/SR-2016/503.

(41) Dickson, J. O.; Mayes, M.; Earles, J. E.; Mehlhorn, T. L.; Lowe, K. A.; Peterson, M. J.; Pierce, E. M. Soil investigation of lower east fork poplar creek. **2017**, 126.

(42) Bloom, N. S.; Preus, E.; Katon, J.; Hiltner, M. Selective extractions to assess the biogeochemically relevant fractionation of inorganic mercury in sediments and soils. *Analytica Chimica Acta* **2003**, *479* (2), 233-248. DOI: https://doi.org/10.1016/S0003-2670(02)01550-7.

(43) Issaro, N.; Abi-Ghanem, C.; Bermond, A. Fractionation studies of mercury in soils and sediments: A review of the chemical reagents used for mercury extraction. *Analytica Chimica Acta* **2009**, *631*, 1-12. DOI: 10.1016/j.aca.2008.10.020.

(44) Kim, C. S.; Bloom, N. S.; Rytuba, J. J.; Brown, G. E. Mercury speciation by x-ray absorption fine structure spectroscopy and sequential chemical extractions: A comparison of speciation methods. *Environmental Science and Technology* **2003**, *37*, 5102-5108. DOI: 10.1021/es0341485.

(45) Leermakers, M.; Baeyens, W.; Quevauviller, P.; Horvat, M. Mercury in environmental samples: Speciation, artifacts and validation. *TrAC Trends in Analytical Chemistry* **2005**, *24* (5), 383-393. DOI: https://doi.org/10.1016/j.trac.2004.01.001.

(46) Sladek, C.; Gustin, M. S. Evaluation of sequential and selective extraction methods for determination of mercury speciation and mobility in mine waste. *Applied Geochemistry* **2003**, *18* (4), 567-576. DOI: https://doi.org/10.1016/S0883-2927(02)00115-4.

(47) Carmichael, J. An investigation of shallow ground-water quality near east fork poplar creek, oak ridge, tennessee. Nashville, 1989; p 55.

(48) Szynkiewicz, A.; Moore, C. H.; Glamoclija, M.; Pratt, L. M. Sulfur isotope signatures in gypsiferous sediments of the estancia and tularosa basins as indicators of sulfate sources, hydrological processes, and microbial activity. *Geochimica et Cosmochimica Acta* **2009**, *73*, 6162-6186. DOI: 10.1016/j.gca.2009.07.009.

(49) Lefticariu, L.; Pratt, L. M.; Ripley, E. M. Mineralogic and sulfur isotopic effects accompanying oxidation of pyrite in millimolar solutions of hydrogen peroxide at temperatures from 4 to 150 °c. *Geochimica et Cosmochimica Acta* **2006**, *70*, 4889-4905. DOI: 10.1016/j.gca.2006.07.026.

(50) Brüchert, V.; Pratt, L. M. Contemporaneous early diagenetic formation of organic and inorganic sulfur in estuarine sediments from st. Andrew bay, florida, USA. *Geochimica et Cosmochimica Acta* **1996**, *60*, 2325-2332. DOI: 10.1016/0016-7037(96)00087-7.

(51) Abràmoff, M. D.; Magalhães, P. J.; Ram, S. J. Image processing with imagej part ii. *Biophotonics International* **2004**, *11*, 36-43.

(52) Schneider, C.; Rasband, W.; Eliceiri, K. Nih image to imagej: 25 years of image analysis. *Nature Methods* **2012**, *9*, 671-675. DOI: 10.1007/978-1-84882-087-6_9.

(53) Hu, H.; Lin, H.; Zheng, W.; Tomanicek, S. J.; Johs, A.; Feng, X.; Elias, D. A.; Liang, L.; Gu, B. Oxidation and methylation of dissolved elemental mercury by anaerobic bacteria. *Nature Geoscience* **2013**, *6*, 751-754. DOI: 10.1038/ngeo1894.

(54) Liu, Y. R.; Lu, X.; Zhao, L.; An, J.; He, J. Z.; Pierce, E. M.; Johs, A.; Gu, B. Effects of cellular sorption on mercury bioavailability and methylmercury production by desulfovibrio desulfuricans nd132. *Environmental Science and Technology* **2016**, *50*, 13335-13341. DOI: 10.1021/acs.est.6b04041.

(55) Zhao, L.; Chen, H.; Lu, X.; Lin, H.; Christensen, G. A.; Pierce, E. M.; Gu, B. Contrasting effects of dissolved organic matter on mercury methylation by geobacter sulfurreducens pca and desulfovibrio desulfuricans nd132. *Environmental Science and Technology* **2017**, *51*, 10468-10475. DOI: 10.1021/acs.est.7b02518.

(56) Ravel, B.; Newville, M. Athena, artemis, hephaestus: Data analysis for x-ray absorption spectroscopy using ifeffit. *Journal of Synchrotron Radiation* **2005**, *12* (4), 537-541. DOI: doi:10.1107/S0909049505012719.

(57) Avellan, A.; Stegemeier, J. P.; Gai, K.; Dale, J.; Hsu-Kim, H.; Levard, C.; O'Rear, D.; Hoelen, T. P.; Lowry, G. V. Speciation of mercury in selected areas of the petroleum value chain. *Environmental Science and Technology* **2018**, *52*, 1655-1664. DOI: 10.1021/acs.est.7b05066.

(58) Pham, A. L. T.; Morris, A.; Zhang, T.; Ticknor, J.; Levard, C. m.; Hsu-Kim, H. Precipitation of nanoscale mercuric sulfides in the presence of natural organic matter: Structural properties, aggregation, and biotransformation. *Geochimica et Cosmochimica Acta* **2014**, *133*, 204-215. DOI: 10.1016/j.gca.2014.02.027.

(59) Wyckoff, R. W. G. *Crystal structures i*; Interscience Publishers, 1963.

(60) Downs, R. T.; Wallace-Hall, M. The american mineralogist crystal structure database. *American Mineralogist* **2003**, *88* (1), 247-250.

(61) Meyer, F.; Paarmann, D.; D'Souza, M.; Olson, R.; Glass, E. M.; Kubal, M.; Paczian, T.; Rodriguez, A.; Stevens, R.; Wilke, A.; et al. The metagenomics rast server - a public resource for the automatic phylogenetic and functional analysis of metagenomes. *BMC Bioinformatics* **2008**, *9*, 1-8. DOI: 10.1186/1471-2105-9-386.

(62) Kent, W. J. Blat---the blast-like alignment tool. *Genome Research* **2002**, *12*, 656-664. DOI: 10.1101/gr.229202.

(63) Wilke, A.; Harrison, T.; Wilkening, J.; Field, D.; Glass, E. M.; Kyrpides, N.; Mavrommatis, K.; Meyer, F. The m5nr: A novel non-redundant database containing protein sequences and annotations from multiple sources and associated tools. *BMC Bioinformatics* **2012**, *13*. DOI: 10.1186/1471-2105-13-141.

(64) Brooks, S.; Eller, V.; Dickson, J.; Earles, J.; Lowe, K.; Mehlhorn, T.; Olsen, T.; Derolph, C.; Watson, D.; Phillips, D.; et al. Mercury content of sediments in east fork poplar creek: Current assessment and past trends. **2017**. DOI: ORNL/TM-2016/578.

(65) Sposito, G. The chemistry of soils. **2008**. DOI: 10.1017/CBO9781107415324.004.

(66) Enescu, M.; Nagy, K. L.; Manceau, A. Nucleation of mercury sulfide by dealkylation. *Scientific Reports* **2016**, *6*, 1-6. DOI: 10.1038/srep39359.

(67) Aiken, G. R.; Hsu-Kim, H.; Ryan, J. N. Influence of dissolved organic matter on the environmental fate of metals, nanoparticles, and colloids. *Environmental Science and Technology* **2011**, *45*, 3196-3201. DOI: 10.1021/es103992s.

(68) Skyllberg, U.; Bloom, P. R.; Qian, J.; Lin, C. M.; Bleam, W. F. Complexation of mercury(ii) in soil organic matter: Exafs evidence for linear two-coordination with reduced sulfur groups. *Environmental Science and Technology* **2006**, *40*, 4174-4180. DOI: 10.1021/es0600577.

(69) Kim, C. S.; Rytuba, J. J.; Brown, G. E. Exafs study of mercury(ii) sorption to fe- and al-(hydr)oxides: I. Effects of ph. *Journal of Colloid and Interface Science* **2004**, *271*, 1-15. DOI: 10.1016/S0021-9797(03)00330-8.

(70) Yang, J.; Ok, Y. S. Kinetics of hg adsorption onto noncrystalline al hydroxide as influenced by low-molecular-weight organic ligands. *Archives of Agronomy and Soil Science* **2017**, *63*.

(71) Farrah, H.; Pickering, W. F. The sorption of mercury species by clay minerals. *Water, Air, and Soil Pollution* **1978**, *9*, 23-31. DOI: 10.1007/BF00185744.

(72) Hofacker, A. F.; Voegelin, A.; Kaegi, R.; Kretzschmar, R. Mercury mobilization in a flooded soil by incorporation into metallic copper and metal sulfide nanoparticles. *Environmental Science and Technology* **2013**, *47*, 7739-7746. DOI: 10.1021/es4010976.

(73) O'Connor, D.; Hou, D.; Ok, Y. S.; Mulder, J.; Duan, L.; Wu, Q.; Wang, S.; Tack, F. M. G.; Rinklebe, J. Mercury speciation, transformation, and transportation in soils, atmospheric flux, and implications for risk management: A critical review. *Environmental International* **2019**, *126*, 747-761. DOI: 10.1016/j.envint.2019.03.019.

(74) Frenkel, A. I.; Hills, C. W.; Nuzzo, R. G. A view from the inside: Complexity in the atomic scale ordering of supported metal nanoparticles. *Journal of Physical Chemistry B* **2001**, *105*, 12689-12703. DOI: 10.1021/jp012769j.

(75) Jentys, A. Estimation of mean size and shape of small metal particles by exafs. *Physical Chemistry Chemical Physics* **1999**, *1*, 4059-4063. DOI: 10.1039/a904654b.

(76) Gregor, R. B.; Lytle, F. Morphology of supported metal clusters: Determination by exafs and chemisorption. *Journal of Catalysis* **1980**, *63*, 476-486.

(77) Gondikas, A. P.; Masion, A.; Auffan, M.; Lau, B. L. T.; Hsu-Kim, H. Early-stage precipitation kinetics of zinc sulfide nanoclusters forming in the presence of cysteine. *Chem Geol* **2012**, *329*, 10-17. DOI: 10.1016/j.chemgeo.2011.06.009.

(78) Marinkovic, N. S.; Sasaki, K.; Adzic, R. R. Determination of single- and multi-component nanoparticle sizes by x-ray absorption spectroscopy. *J Electrochem Soc* **2018**, *165* (15), J3222-J3230. DOI: 10.1149/2.0281815jes.

(79) Eskelsen, J. R.; Xu, J.; Chiu, M.; Moon, J. W.; Wilkins, B.; Graham, D. E.; Gu, B.; Pierce, E. M. Influence of structural defects on biomineralized zns nanoparticle dissolution: An in-situ electron microscopy study. *Environmental Science and Technology* **2018**, *52*, 1139-1149. DOI: 10.1021/acs.est.7b04343.

(80) Ischenko, V.; Polarz, S.; Grote, D.; Stavarache, V.; Fink, K.; Driess, M. Zinc oxide nanoparticles with defects. *Advanced Functional Materials* **2005**, *15*, 1945-1954. DOI: 10.1002/adfm.200500087.

(81) Langille, M. R.; Personick, M. L.; Zhang, J.; Mirkin, C. A. Defining rules for the shape evolution of gold nanoparticles. *Journal of the American Chemical Society* **2012**, *134*, 14542-14554. DOI: 10.1021/ja305245g.

(82) Xu, J.; Murayama, M.; Roco, C. M.; Veeramani, H.; Michel, F. M.; Rimstidt, J. D.; Winkler, C.; Hochella, M. F. Highly-defective nanocrystals of zns formed via dissimilatory bacterial sulfate reduction: A comparative study with their abiogenic analogues. *Geochimica et Cosmochimica Acta* **2016**, *180*, 1-14. DOI: 10.1016/j.gca.2016.02.007.

(83) Zhang, J.; Lin, Z.; Lan, Y.; Ren, G.; Chen, D.; Huang, F.; Hong, M. A multistep oriented attachment kinetics: Coarsening of zns nanoparticle in concentrated naoh. *Journal of the American Chemical Society* **2006**, *128*, 12981-12987. DOI: 10.1021/ja062572a.

(84) Manceau, A.; Lemouchi, C.; Rovezzi, M.; Lanson, M.; Glatzel, P.; Nagy, K. L.; Gautier-Luneau, I.; Joly, Y.; Enescu, M. Structure, bonding, and stability of mercury complexes with thiolate and thioether ligands from high-resolution xanes spectroscopy and first-principles calculations. *Inorganic Chemistry* **2015**, *54*, 11776-11791. DOI: 10.1021/acs.inorgchem.5b01932.

(85) Luo, H. W.; Yin, X.; Jubb, A. M.; Chen, H.; Lu, X.; Zhang, W.; Lin, H.; Yu, H. Q.; Liang, L.; Sheng, G. P.; et al. Photochemical reactions between mercury (hg) and dissolved organic matter decrease hg bioavailability and methylation. *Environmental Pollution* **2017**, *220*, 1359-1365. DOI: 10.1016/j.envpol.2016.10.099.

(86) Müller, A. L.; Kjeldsen, K. U.; Rattei, T.; Pester, M.; Loy, A. Phylogenetic and environmental diversity of dsrab-type dissimilatory (bi)sulfite reductases. *ISME Journal* **2015**, *9*, 1152-1165. DOI: 10.1038/ismej.2014.208.

(87) Canfield, D. E. Biogeochemistry of sulfur isotopes. *Reviews in Mineralogy and Geochemistry* **2001**, *43* (1), 607-636. DOI: 10.2138/gsrmg.43.1.607 %J Reviews in Mineralogy and Geochemistry (acccessed 6/20/2021).

(88) Ramsey, A. B.; Szynkiewicz, A. Coupled chemical-isotope assessment of potential metal releases to the water column from river sediments impacted by coal ash spill. *Applied Geochemistry* **2019**, *107*, 34-44. DOI: https://doi.org/10.1016/j.apgeochem.2019.05.016.

(89) Philippe, A.; Schaumann, G. E. Interactions of dissolved organic matter with natural and engineered inorganic colloids: A review. *Environmental Science & Technology* **2014**, *48* (16), 8946-8962. DOI: 10.1021/es502342r.

(90) Deonarine, A.; Hsu-Kim, H. Precipitation of mercuric sulfide nanoparticles in nom-containing water: Implications for the natural environment. *Environmental Science and Technology* **2009**, *43*, 2368-2373. DOI: 10.1021/es803130h.

(91) Slowey, A. J. Rate of formation and dissolution of mercury sulfide nanoparticles: The dual role of natural organic matter. *Geochimica et Cosmochimica Acta* **2010**, *74*, 4693-4708. DOI: 10.1016/j.gca.2010.05.012.

(92) Poulin, B. A.; Gerbig, C. A.; Kim, C. S.; Stegemeier, J. P.; Ryan, J. N.; Aiken, G. R. Effects of sulfide concentration and dissolved organic matter characteristics on the structure of nanocolloidal metacinnabar. *Environmental Science and Technology* **2017**, *51*, 13133-13142. DOI: 10.1021/acs.est.7b02687.

(93) Charnock, J. M.; Moyes, L. N.; Pattrick, R. A. D.; Mosselmans, J. F. W.; Vaughan, D. J.; Livens, F. R. The structural evolution of mercury sulfide precipitate: An xas and xrd study. *American Mineralogist* **2003**, *88*, 1197-1203. DOI: 10.2138/am-2003-8-903.

(94) Rytuba, J. J. Mercury from mineral deposits and potential environmental impact. *Environmental Geology* **2003**, *43*, 326-338. DOI: 10.1007/s00254-002-0629-5.

(95) Gray, J. E.; Theodorakos, P. M.; Bailey, E. A.; Turner, R. R. Distribution, speciation, and transport of mercury in stream-sediment, stream-water, and fish collected near abandoned mercury mines in

southwestern alaska, USA. *Science of the Total Environment* **2000**, *260*, 21-33. DOI: 10.1016/S0048-9697(00)00539-8.

(96) Gehrke, G. E.; Blum, J. D.; Marvin-DiPasquale, M. Sources of mercury to san francisco bay surface sediment as revealed by mercury stable isotopes. *Geochimica et Cosmochimica Acta* **2011**, *75*, 691-705. DOI: 10.1016/j.gca.2010.11.012.

(97) Lechler, P. J.; Miller, J. R.; Hsu, L. C.; Desilets, M. O. Mercury mobility at the carson river superfund site, west-central nevada, USA: Interpretation of mercury speciation data in mill tailings, soils, and sediments. *Journal of Geochemical Exploration* **1997**, *58*, 259-267. DOI: 10.1016/S0375-6742(96)00071-4.

(98) Eckley, C. S.; Luxton, T. P.; McKernan, J. L.; Goetz, J.; Goulet, J. Influence of reservoir water level fluctuations on sediment methylmercury concentrations downstream of the historical black butte mercury mine, or. *Applied Geochemistry* **2015**, *61*, 284-293. DOI: 10.1016/j.apgeochem.2015.06.011.

(99) Curtis, L. Sources and chronology of mercury contamination in cottage grove reservoir. Portland, 2005; p 39.

(100) Niane, B.; Guédron, S.; Feder, F.; Legros, S.; Ngom, P. M.; Moritz, R. Impact of recent artisanal small-scale gold mining in senegal: Mercury and methylmercury contamination of terrestrial and aquatic ecosystems. *Science of The Total Environment* **2019**, *669*, 185-193. DOI: https://doi.org/10.1016/j.scitotenv.2019.03.108.

(101) Diringer, S.; Feingold, B. J.; Ortiz, E. J.; Gallis, J. A.; Arauo-Flores, J. M.; Berky, A.; Pan, W. K. Y.; Hsu-kim, H. River transport of mercury from artisanal and small-scale gold mining and risks for dietary mercury exposure in madre de dios , peru †. *Environmental Science Processes & Impacts* **2015**, *17*, 478-487. DOI: 10.1039/C4EM00567H.

(102) Goix, S.; Maurice, L.; Laffont, L.; Rinaldo, R.; Lagane, C.; Chmeleff, J.; Menges, J.; Heimbürger, L. E.; Maury-Brachet, R.; Sonke, J. E. Quantifying the impacts of artisanal gold mining on a tropical river system using mercury isotopes. *Chemosphere* **2019**, *219*, 684-694. DOI: 10.1016/j.chemosphere.2018.12.036.

(103) Zhang, T.; Kim, B.; Levard, C.; Reinsch, B. C.; Lowry, G. V.; Deshusses, M. A.; Hsu-Kim, H. Methylation of mercury by bacteria exposed to dissolved, nanoparticulate, and microparticulate mercuric sulfides. *Environmental Science & Technology* **2012**, *46* (13), 6950-6958. DOI: 10.1021/es203181m.

(104) Graham, A. M.; Aiken, G. R.; Gilmour, C. C. Dissolved organic matter enhances microbial mercury methylation under sulfidic conditions. *Environmental Science & Technology* **2012**, *46* (5), 2715-2723. DOI: 10.1021/es203658f.

(105) Mansor, M.; Xu, J. Benefits at the nanoscale: A review of nanoparticle-enabled processes favouring microbial growth and functionality. *Environmental Microbiology* **2020**, *22*, 3633-3649. DOI: 10.1111/1462-2920.15174.

(106) Bakshi, S.; He, Z. L.; Harris, W. G. Natural nanoparticles: Implications for environment and human health. *Critical Reviews in Environmental Science and Technology* **2015**, *45*, 861-904. DOI: 10.1080/10643389.2014.921975.

(107) Banfield, J. F.; Zhang, H. Nanoparticles in the environment. *Reviews in Mineralogy and Geochemistry* **2001**, *44*, 1-58. DOI: 10.2138/rmg.2001.44.01.

(108) Gilbert, B.; Huang, F.; Zhang, H.; Waychunas, G. A.; Banfield, J. F. Nanoparticles: Strained and stiff. *Science* **2004**, *305*, 651-654. DOI: 10.1126/science.1098454.

(109) He, H.; Cao, J.; Duan, N. Defects and their behaviors in mineral dissolution under water environment: A review. *Science of the Total Environment* **2019**, *651*, 2208-2217. DOI: 10.1016/j.scitotenv.2018.10.151.

(110) Shen, Z.; Zhang, Z.; Li, T.; Yao, Q.; Zhang, T.; Chen, W. Facet-dependent adsorption and fractionation of natural organic matter on crystalline metal oxide nanoparticles. *Environmental Science and Technology* **2020**, *54*, 8622-8631. DOI: 10.1021/acs.est.9b06111.

(111) Huang, X.; Hou, X.; Song, F.; Zhao, J.; Zhang, L. Ascorbate induced facet dependent reductive dissolution of hematite nanocrystals. *Journal of Physical Chemistry C* **2017**, *121*, 1113-1121. DOI: 10.1021/acs.jpcc.6b09281.

(112) Huang, X.; Hou, X.; Zhang, X.; Rosso, K. M.; Zhang, L. Facet-dependent contaminant removal properties of hematite nanocrystals and their environmental implications. *Environmental Science: Nano* **2018**, *5*, 1790-1806. DOI: 10.1039/c8en00548f.

(113) Tian, L.; Guan, W.; Ji, Y.; He, X.; Chen, W.; Alvarez, P. J. J.; Zhang, T. Microbial methylation potential of mercury sulfide particles dictated by surface structure. *Nature Geoscience* **2021**. DOI: 10.1038/s41561-021-00735-y.

(114) Crowther, E. R.; Demers, J. D.; Blum, J. D.; Brooks, S. C.; Johnson, M. W. Use of sequential extraction and mercury stable isotope analysis to assess remobilization of sediment-bound legacy mercury. *Environmental Science: Processes & Impacts* **2021**, *23* (5), 756-775, 10.1039/D1EM00019E. DOI: 10.1039/D1EM00019E.

(115) Demers, J. D.; Blum, J. D.; Brooks, S. C.; Donovan, Patrick M.; Riscassi, A. L.; Miller, C. L.; Zheng, W.; Gu, B. Hg isotopes reveal in-stream processing and legacy inputs in east fork poplar creek, oak ridge, tennessee, USA. *Environmental Science: Processes & Impacts* **2018**, *20* (4), 686-707, 10.1039/C7EM00538E. DOI: 10.1039/C7EM00538E.

(116) Shrihari; Modak, J. M.; Kumar, R.; Gandhi, K. S. Dissolution of particles of pyrite mineral by direct attachment of thiobacillus ferrooxidans. *Hydrometallurgy* **1995**, *38*, 175-187. DOI: 10.1016/0304-386X(94)00053-6.